

Bulk gold with hierarchical macro-, micro- and nano-porosity

Marie E. Cox, David C. Dunand*

Department of Materials Science and Engineering, Northwestern University, 2220 Campus Drive, Evanston, IL, 60208, USA

ARTICLE INFO

Article history:

Received 9 October 2010
 Received in revised form
 10 November 2010
 Accepted 22 November 2010
 Available online 30 November 2010

Keywords:

Gold
 Porous materials
 Mechanical characterization
 Nanoporous
 Hierarchical foam
 Powder metallurgy

ABSTRACT

Millimeter-sized, free-standing gold structures were created with three levels of multiscale porosity. First, macro- and microporosity, which are useful for mass and heat transport within the structure, are formed within an Ag–19 at.% Au alloy by salt powder replication during powder densification and by entrapped gas expansion during sintering, respectively. Nanoporosity, which provides high surface area, is then produced by silver dealloying of these Ag–19 at.% Au foams. The resulting hierarchical gold structures are annealed at 100–800 °C, thus coarsening the ligaments, increasing relative density, and healing cracks produced during dealloying. The first effect weakens the structure, while the other two make it stronger. A bulk Au sample with hierarchical porosity annealed at 600 °C shows good compressive ductility and a strength in agreement with models.

© 2010 Elsevier B.V. All rights reserved.

1. Introduction

Nanoporous gold (np-Au) has recently attracted interest due to its novel mechanical, optical, catalytic and sensing properties [1–4]. Creation of hierarchically sized porosity is of interest for applications in catalysis, biosensing [5] and surface-enhanced Raman scattering [6]. For example, micropores facilitate mass transport while nanopores increase surface area. A number of methods to produce hierarchical np-Au thin films have been published [7–12], but there has been limited work on bulk (millimeter-sized) self-supporting hierarchical nanoporous metals. Nyce et al. [13] described a method to create gold structures with hierarchical porosity by templating 9.6 mm diameter polystyrene spheres with Ag–Au powders, slip casting and annealing (thus densifying the powders and removing the polystyrene spheres), and finally dealloying the less noble Ag from the hollow Ag–Au spheres. The resulting structure had two levels of porosity: an assembly of partially sintered 5 μm hollow spheres with Au walls exhibiting 10–100 nm nanopores [13]. Another method used deposition of Au nanoparticles onto porous silicon diatom frustules replicas followed by selective dissolution of the silicon template to create individual, micron-sized structures with complex micro- and nanopores (0.5–10 μm and 10–300 nm in size, respectively) [14]. Finally, Au nanoparticle have been found to self assemble into a network of tubes (with 1.3 μm diameter and

0.2 μm thick walls) consisting of partially bonded Au nanoparticles [15].

None of the three studies reviewed above have reported on the mechanical properties of their hierarchical gold structures. The mechanical properties of dealloyed np-Au have been a topic of interest for the near-theoretical yield strengths (1.5–4.3 GPa) exhibited by individual Au ligaments (10–15 nm diameter), as determined from compression of micropillars or nanoindentation of np-Au [16,17]. Most mechanical testing of np-Au has been limited to the microscale [16,17] because of the difficulties associated with producing bulk samples of np-Au free of cracks resulting from the shrinkage occurring during conventional dealloying processes [18]. Only a few studies have reported mechanical properties of bulk (millimeter-size) np-Au samples. Li and Sieradzki [19] created 2 mm × 2 mm × 30 mm np-Au beams for 3-point bend testing by dealloying of cast Ag–24 at.% Au samples, and coarsened their nanoligaments by annealing for 10 min at various temperatures. For 100 and 300 °C annealing temperatures, the samples were brittle, but as the annealing temperature increased from 400 to 800 °C, plastic bending deflection and fracture stresses increased, indicating a size-defined ductile-to-brittle transition. However, the authors did not report the sample density, which probably increased as well with annealing temperature. Recently, Jin et al. [20] successfully prepared crack-free, millimeter-sized (1 mm × 1 mm × 2 mm) np-Au samples with a polycrystalline microstructure by slowing the dealloying process on an Ag–25 at.% Au alloy, using a lower potential and a higher temperature than conventional methods. Also, Balk et al. [21] dealloyed Ag–30 at.% Au dog-bone specimens from cold-rolled and annealed plates, with a gauge length of ~430 μm

* Corresponding author. Tel.: +1 847 491 5370; fax: +1 847 467 6573.
 E-mail address: dunand@northwestern.edu (D.C. Dunand).

and thicknesses of 30–400 μm for compression and tension testing. In both studies, np-Au in bulk form was much weaker than np-Au in micropillar forms, which was thought to be caused by accumulation of ‘pore channel dislocations’ causing stress concentrations [20].

Here, we present a novel processing technique that produces a bulk (i.e., self-supported, millimeter-sized) gold structure with three hierarchical levels of porosity: macro-, micro- and nanoporosity, produced respectively by salt replication, gas expansion and dealloying of Ag. Ligament size effects on compressive strength and ductility of these gold structures with hierarchical porosities are studied by coarsening the microstructure at various temperatures.

2. Experimental procedures

Spherical elemental Ag and Au powders (1.3–3.2 μm , Alfa Aesar) were blended with a 2.3:1 mass ratio, corresponding to an average Ag–30 wt.% Au (Ag–19 at.% Au) composition. The powder blend was then mixed with 50 vol.% NaCl (300–355 μm , Alfa Aesar) in air, and uniaxially cold-pressed into a 3.2 mm diameter die at a pressure of 450 MPa for 10 min. The resulting Ag–Au–NaCl cylinders (with 7–7.5 mm height) were heated at a rate of 5 $^{\circ}\text{C}/\text{min}$ to 770 $^{\circ}\text{C}$ (below the 801 $^{\circ}\text{C}$ melting point of NaCl) and maintained at this temperature for a time $t = 50$ h under vacuum (with 10 mTorr residual pressure). The corresponding diffusion distance is $\sim(Dt)^{1/2} = 55\text{--}58$ μm (where $D = 1.7\text{--}1.9 \times 10^{-14}$ m^2/s at 770 $^{\circ}\text{C}$ is the interdiffusion coefficient in the Ag–Au system [22]), which is much larger than the powder size, insuring full chemical homogenization between the Au and Ag powders. NaCl was then removed by dissolution from the homogenized Ag–Au samples by suspending the whole sample in agitated deionized water at 100 $^{\circ}\text{C}$ for 40–60 h. NaCl removal was confirmed by mass loss measurements. Fig. 1 shows a representative cross-section of the samples at this point in the processing. The Ag–19 at.% Au matrix exhibits both macroscopic porosity (from NaCl) and microscopic porosity (from expansion of entrapped water vapor, as discussed in more details later). The cylinders (which had expanded to a 3.3 mm diameter) were polished to a $\sim 2.2:1$ height-to-diameter ratio, and their porosity was measured using He pycnometry and the Archimedes method.

To create nanoporosity, silver was selectively dealloyed from the porous Ag–Au cylinders by immersion in HNO_3 aqueous solutions of increasing concentrations (25% for 24 h, 50% for 40 h and 75% for 12 h). Samples were rinsed with deionized water 7–8 times after dealloying was completed, air-dried for 24 h and weighted to quantify the Ag removal. Finally, four dealloyed Au samples were annealed for 30 min at 100, 300, 600 or 800 $^{\circ}\text{C}$ to coarsen the np-Au ligaments. These coarsened porous Au cylinders were uniaxially compressed under displacement control at a nominal strain rate of 5×10^{-4} s^{-1} . Strain was measured by cross-head displacement, taking into account load train compliance determined on aluminum calibration samples before and after each test. Fracture surfaces were imaged using a Hitachi S-4800 FE-SEM.

3. Results and discussion

3.1. Macro- and microporosity

Optical micrographs taken after sintering and removal of NaCl space holders from the Ag–19 at.% Au matrix show blocky macropores (300–350 μm) replicating the shape and size of the NaCl particles (Fig. 1a). The microporosity ranges from small, 0.5 μm spheroidal pores to irregularly shaped pores, up to 60 μm in their long dimension (Fig. 1b). These micropores could be generated reproducibly in control experiments, albeit with variable size and

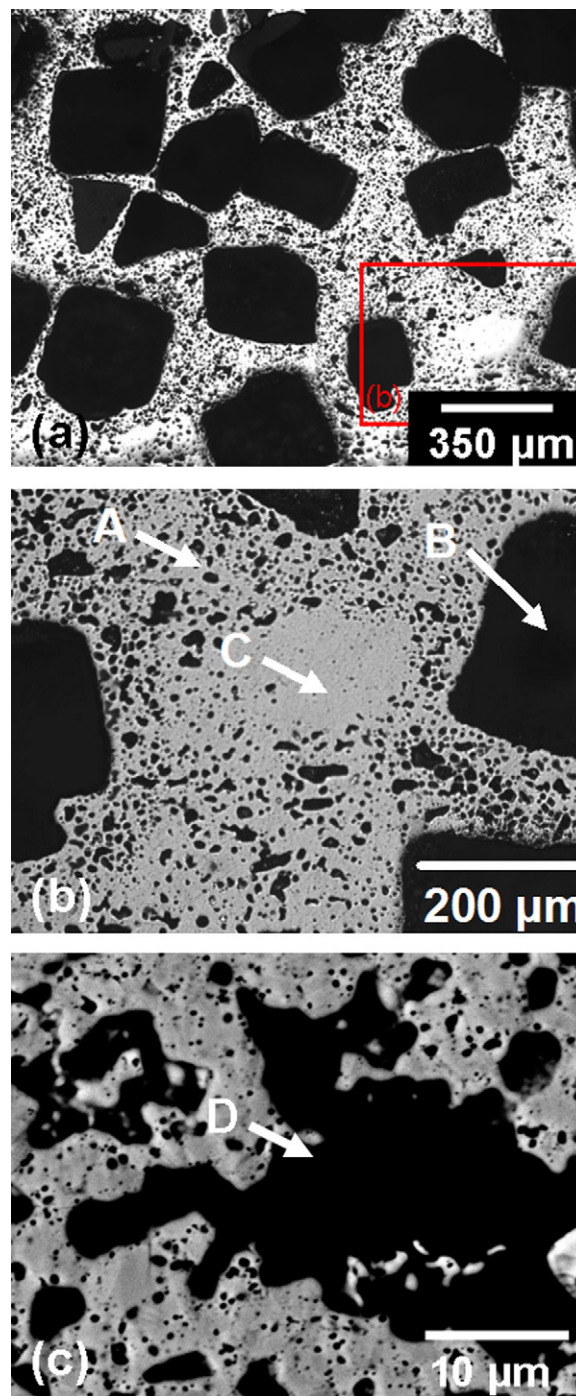


Fig. 1. Polished cross sections of Ag–19 at.% Au structure after sintering and NaCl removal, but before dealloying. (a) Low magnification optical micrograph showing macropores (300–350 μm , darker blocky features) produced by salt replication; (b) higher magnification optical micrograph showing 1–60 μm micropores (A), produced by vapor expansion within the ligaments surrounding the macropores (B); also visible is a region (C) free of microporosity. (c) SEM micrograph showing a larger micropore (D) created by merging of multiple smaller micropores.

number density. They are created by expansion of entrapped gas, most probably water, which is consistent with the swelling of the samples to a 3.3 mm diameter, rather than the shrinkage expected from powder sintering. While water was not added to the Ag–Au–NaCl powder mixture, it was present in the highly hygroscopic NaCl handled in laboratory air. Most likely, during initial heating of the green samples to the sintering treatment, water vapor was released from the NaCl powders starting at ~ 100 $^{\circ}\text{C}$ and

permeated the surrounding packed preform of Ag and Au powders. Some of the vapor was trapped as the Ag–Au preform sintered upon slow heating (5 °C/min) to the sintering temperature of 770 °C. At that temperature, the entrapped water vapor expanded by creep of the surrounding matrix during the 50 h heat-treatment used to insure homogenization of the alloy. Fig. 1c shows features that were created by the merging of individual micropores during the homogenization process. A similar process has been used to create up to 44% porosity in Ti [23,24] and up to 20% in NiTi [25,26] by trapping and expansion of Ar, and these study also report the same type of elongated pores as seen in Fig. 1c, resulting of merging of neighboring equiaxed pores which connected with each other and the specimen surface to result in open porosity. While Kirkendall porosity is created during the interdiffusion process between gold and silver [27], the size of the Kirkendall pores is expected to be smaller than the Ag and Au powder size (1–3 μm) and thus much smaller than the micropores present in our structures. Kirkendall pores, if they formed during our annealing process, probably disappeared through the Gibbs–Thomson effect [27] as vacancies diffused from the Kirkendall pores to the nearby micro- and macropores.

As illustrated in Fig. 1b, limited microporosity is visible in matrix regions far from the NaCl powders, confirming that these were the sources of water vapor. After removal of NaCl, the samples exhibit 59–65% open porosities and a low value (<1%) of closed porosities (Table 1), indicating that the micropores are connected to the macropores. Given the initial 50 vol.% NaCl used in the powder blends, it can be concluded that the macroporosity (from NaCl) represents 50% and the microporosity (from gas) 9–15% of the total Ag–Au volume.

In addition to the micro- and macroporosity created by salt replication and vapor expansion, micron-sized spherical features are observed using SEM on the interior surfaces of the macropores and larger micropores. These 1–5 μm spherical features have the same size range as the elemental powder size (1.3–3.2 μm) used to create Ag–19 at.% Au matrix and may thus represent prior powders. These features were also observed after the selective dealloying of Ag, before and after coarsening (Fig. 2).

3.2. Nanoporous structures

The gold ligaments resulting from dealloying of the Ag–19 at.% Au structures had apparent diameters of 25–100 nm (Fig. 3). After the dealloying process, the samples were very brittle and they exhibited small cracks on their surfaces. Macro-defects in dealloyed np-Au foils are a common occurrence attributed to the large volume shrinkage (up to 30%) during dealloying [28]. Initial attempts to dealloy the present Ag–Au samples in a single step with 75% HNO₃ [29] resulted in catastrophic cracking of the samples. The multi-step dealloying procedure described above resulted in the fewest surface cracks. There was also a reduction in the number of surface cracks after annealing at 100 °C, and this healing continued with increasing annealing temperature from 300 to 600 and 800 °C.

Table 1

Sample porosities before and after dealloying final ligament diameters after annealing, yield strengths measured by compression and predicted yield strengths of nanoligaments from Eq. (2) ($a = 45 \text{ GPa nm}^{0.86}$) and of hierarchical structure from Eq. (6) ($C_2 = 0.3$).

Annealing temperature (°C)	Before dealloying		After dealloying and annealing			Yield strength (MPa)		
	Open porosity (%)	Closed porosity foam (%)	Shrinkage (%)	Total porosity (%)	Ligament diameter (nm)	Foam (experimental)	Ligament: σ_L^{YS} (Eq. (2))	Foam: σ_h (Eq. (6))
100	65 ± 0.2	0.7 ± 1.2	4	89 ± 0.3	44 ± 14	0.31 ± 0.08	1757	5.8
300	64 ± 0.2	1.7 ± 0.5	8.9	84 ± 1.4	124 ± 58	0.97 ± 0.12	733	4.2
600	59 ± 0.4	2.1 ± 0.8	17.8	74 ± 0.4	138 ± 36	5.64 ± 0.64	670	8
800	63 ± 0.1	2.3 ± 1.3	23.8	69 ± 0.01	2226 ± 681	6.30 ± 0.31	79	1.2

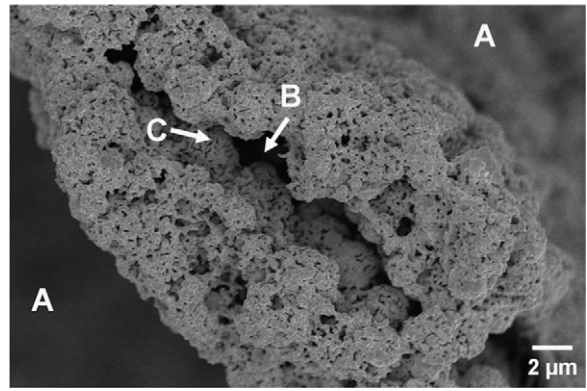


Fig. 2. SEM images of fracture surface of compression sample of hierarchical Au structure annealed at 600 °C. Spherical structures (C) are present on each side of the cell walls separating the macropores (A) and micropores (B).

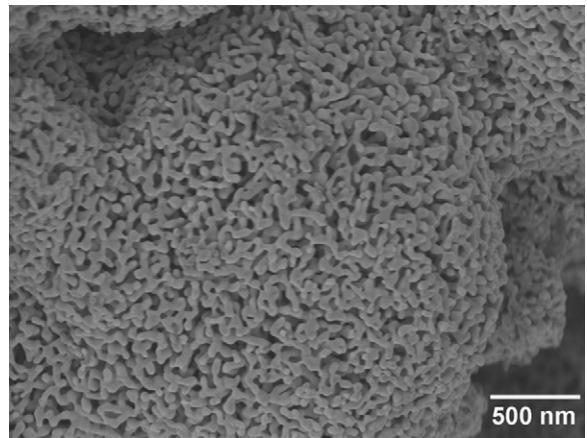


Fig. 3. SEM image of fracture surface of dealloyed hierarchical Au structure (no annealing) showing nanopores and nano-ligaments.

Due to the fragile nature of the samples, their densities were calculated from mass and dimensions determined with a calibrated optical microscopy. Shrinkage due to annealing was found as the difference between the measured relative density of the sample and the expected relative density assuming no change in sample dimension from dealloying or annealing. This expected relative density was calculated by multiplying the relative density found before dealloying with the relative density of 0.19 (19%) expected for np-Au created without shrinkage from an Ag–19 at.% Au alloy. As shown in Table 1, the samples annealed at 100 and 300 °C show a relatively small volumetric shrinkage of 4–9% corresponding to a linear shrinkage of ~1–3%. Annealing at 600 and 800 °C leads to volumetric shrinkages of 18 and 24% (linear shrinkage of 6 and 8%), as expected given that these are high homologous temperatures (65 and 80% of the absolute melting point of gold). SEM observation of fracture surfaces, after mechanical testing, showed a

reduction in microporosity with increasing annealing temperature. Densification may also have occurred at the level of the nanopores.

SEM images also illustrate the coarsening of the Au ligaments with increasing annealing temperature (Fig. 4a–d). For the samples annealed at 100, 300 and 600 °C (Fig. 4a–c), the ligaments are clearly distinguishable and their diameters are within, or close to, the nanoscale (Table 1). Annealing at 800 °C (Fig. 4d) results in micron-size ligaments ($2.2 \pm 0.7 \mu\text{m}$ in size) which are no longer smooth and easily distinguishable. This drastic increase of ligament diameter results in a reduction in surface area and surface curvature which are expected to affect adversely catalytic behavior [2].

3.3. Stress–strain curves of Au with hierarchical porosity

Fig. 5 shows the engineering compressive stress–strain curves for all of the annealed samples. The sample annealed at 100 °C (89% porous, with $44 \pm 14 \text{ nm}$ Au ligaments) was very weak with a yield strength below 0.5 MPa (Fig. 5). The small surface cracks observed before testing, developed into a large crack that was oriented at $\sim 45^\circ$ to the direction of loading (along plane of maximum shear stress) and that propagated across the full width of the sample. After 5% strain, the upper portion of the sample started to be visibly offset from the lower portion, and the sample failed completely at a strain of 16%. The sample annealed at 300 °C (84% porous, with $124 \pm 58 \text{ nm}$ ligaments) had an improved yield strength of $\sim 1 \text{ MPa}$ and large surface cracks were not visible during compression. The plateau region of the stress–strain curve shows serrations because large fragments split from the bottom of the sample and were pushed aside during compression until the test was ended at a strain of 73%.

Annealing at 600 °C lead to significant shrinkage and increase in relative density. The sample (74% porous, with $138 \pm 36 \text{ nm}$ ligaments) is, with a yield strength of 5.6 MPa, significantly stronger than the previously discussed samples. The stress–strain curve has features characteristic of ductile foams in compression, including a long plateau region ($\sim 4 \text{ MPa}$) followed by densification beginning at 60% strain. Similar to the sample annealed at 300 °C, the sample fractured from the bottom and large fragments spall off from the sample.

The 800 °C annealed sample (69% porous, $2.2 \pm 0.7 \mu\text{m}$ ligaments) shows a stress–strain curve characteristic of a ductile foam during compression (Fig. 5). Initial elastic deformation (with a true yield point at 5.3 MPa and a 0.2% offset yield stress at 6.3 MPa) is followed by a gradual transition to plastic deformation at which point the stress was 17 MPa. The sample has a plateau strength of 21 MPa and begins to densify at $\sim 50\%$ strain. During compression, the sample barreled and no spalling or cracking was observed. The improvement in ductility with increasing annealing temperatures visible in Fig. 5 may be due to the healing of cracks formed during dealloying, and/or an increase in the relative density of the sample due to sintering. The increase of ductility is not believed to be linked to the increase in ligament diameter in the np-Au, as Jin et al. [20] have shown that bulk, crack-free samples of np-Au show compressive ductility with strains up to 80% even with ligament diameters as small as 15 nm.

3.4. Modeling structure strength

Fig. 6 shows the measured yield strengths of the annealed samples as a function of their relative density. With the increase in annealing temperature, the ligament diameter increases and the total porosity decreases due to shrinkage of the sample. The Gibson–Ashby model for metallic foams [30] predicts a foam yield strength σ^* of:

$$\sigma^* = C_2(1 - P)^{3/2} \sigma_s^{YS} \quad (1)$$

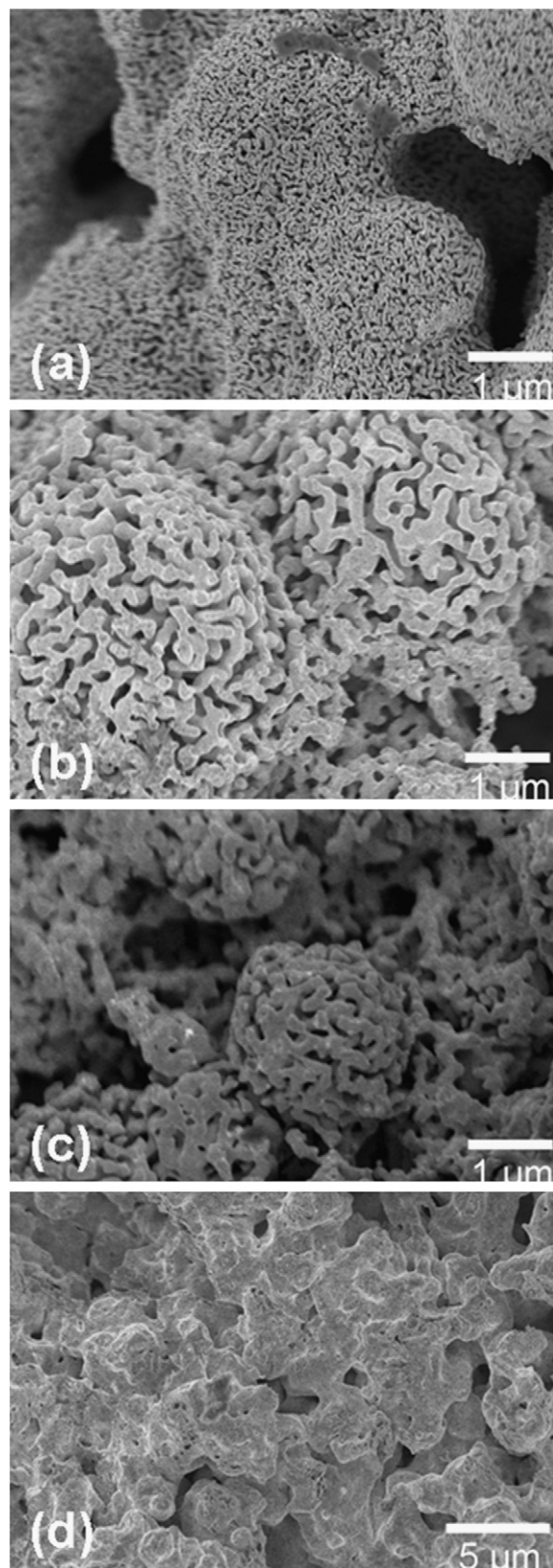


Fig. 4. SEM image of fracture surface of compression samples of hierarchical Au structures annealed before deformation at (a) 100 °C, (b) 300 °C, (c) 600 °C, (d) 800 °C, showing the evolution of ligament and pore size.

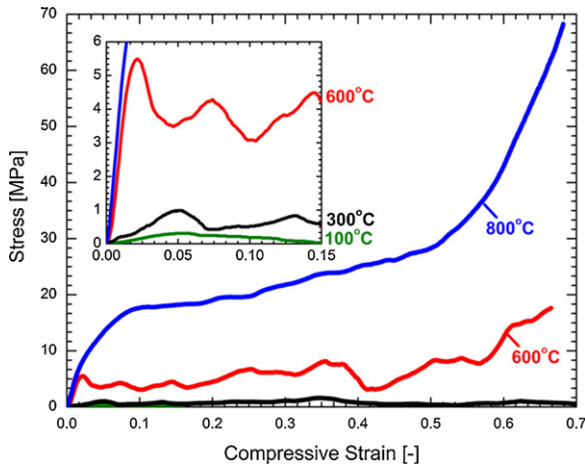


Fig. 5. Compressive stress–strain curves for all hierarchical Au structures, labeled with their annealing temperatures.

where σ_s^{YS} denotes the yield strength of the bulk material, P is the porosity of the foams (with $1 - P$ as the relative density) and the coefficient C_2 is 0.3 ± 0.15 . Using the yield stress of bulk, annealed gold $\sigma_s^{YS} = 85$ MPa (calculated by dividing with a factor 3 the hardness of annealed gold wires [31]), Fig. 6 shows that the experimental results are close to the predictions from Eq. (1) and within the uncertainty associated with C_2 . This agreement is probably fortuitous, since Eq. (1) does not take into account the hierarchical microstructure of the porosity in these structures, nor the change in yield stress of gold associated with the nanometric size of the ligaments.

In np-Au without micro- or macro-pores, the yield strength is dependent on the ligament diameter [32]. Using experimental data from a number of sources, Fan and Fang [33] developed an expression linking the ligament yield strength (σ_L^{YS} expressed in GPa) and the ligament diameter (L expressed in nm):

$$\sigma_L^{YS} = 0.020 + aL^{-0.86} \quad (2)$$

where $a = 45 \text{ GPa nm}^{0.86}$ is a best-fit constant determined from data for ligaments with diameters between 10 nm and $10 \mu\text{m}$. Within the narrower range of diameters relevant to the present structures ($L = 40\text{--}3000$ nm), all data are contained within a band found by replacing a in the above equation with a lower bound value $a/2 = 22.5 \text{ GPa nm}^{0.86}$ and a higher bound $2a = 90 \text{ GPa nm}^{0.86}$.

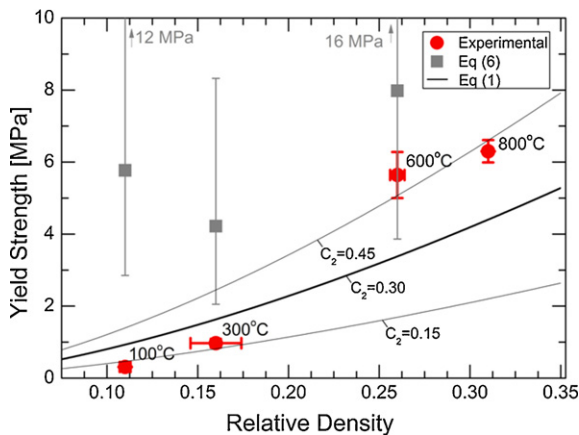


Fig. 6. Plot of compressive yield strength vs. relative density for hierarchical Au structures annealed at various temperatures. Experimental data are shown as circles, predictions from the Gibson–Ashby scaling law (Eq. (1)) as lines, and predictions from the hierarchical strength model (Eq. (6)) as squares, with error bars taking into account the uncertainty in the parameter a in Eq. (2).

The yield strength σ_{np} of the np-Au material, which makes up the walls between the micro-/macropores, is then found by introducing Eq. (2) into Eq. (1):

$$\sigma_{np} = C_2(1 - P_{np})^{3/2}(0.020 + aL^{-0.86}) \quad (3)$$

where P_{np} is the porosity within the np-Au ligaments.

The hierarchical structure is now modeled as a porous material (with a yield strength given by Eq. (1)) consisting of np-Au (with strength given by Eq. (3)) containing macro-/microporosity. Introducing Eq. (3) into Eq. (1) then provides the yield stress σ_h for the hierarchical porous structure:

$$\sigma_h = C_2^2(1 - P_{mm})^{3/2}(1 - P_{np})^{3/2}(0.020 + aL^{-0.86}) \quad (4)$$

where P_{mm} is the porosity associated with only the macro/microporosity in the sample.

Eq. (4) can be further simplified when the nanoporosity within the ligaments, P_{np} , is written in terms of the total porosity P_{total} and the macro/microporosity P_{mm} as:

$$P_{np} = \frac{P_{total} - P_{mm}}{1 - P_{mm}} \quad (5)$$

Substituting Eq. (5) into Eq. (4) and simplifying terms then gives the yield stress of the hierarchical structure as:

$$\sigma_h = C_2^2(1 - P_{total})^{3/2}(0.020 + aL^{-0.86}) \quad (6)$$

Thus, according to this simplified model, the yield stress of the hierarchical porosity structure is dependent only on the total porosity, not on its break-down into nano- and micro/macroporosity. An alternate equation derived by Lakes [34] for hierarchical structures, also based on the Gibson–Ashby models for metallic foams [30], was not used here; this is because that model, which iterates the stiffness of the material to account for structural hierarchy, assumes that yield strain for every level of porosity is equal to the yield strain for the solid material, an assumption which is difficult to justify here since the yield stress (and thus the yield strain) is dependent on feature size.

Fig. 6 shows the yield strengths for the structures with hierarchical porosity calculated using Eq. (6) using $a = 45 \text{ GPa nm}^{0.86}$. As described above, this parameter has a large error, estimated as a factor 2 based on the fit of Eq. (2) to the data points in Ref. [33]. Fig. 6 reflects the fitting error with error bars on the calculated yield stress determined from Eq. (6) with $2a = 90 \text{ GPa nm}^{0.86}$ (upper bound) and $a/2 = 22.5 \text{ GPa nm}^{0.86}$ (lower bound). Predictions for the sample annealed at 800°C are not plotted in Fig. 6 because the nanopores coarsened to the micrometer range (Table 1, Fig. 4d). For this sample, the measured yield stress can be compared to Eq. (1), and there is indeed agreement within the error associated with the parameter C_2 ($C_2 = 0.3 \pm 0.15$).

For the samples annealed at 100 and 300°C , Eq. (6) predicts yield strengths significantly larger than those found experimentally (Fig. 6). A likely explanation for this discrepancy is the presence of cracks developed in the sample during dealloying, which lead to early failure and thus abnormally low yield stresses. Another possible cause is the large errors associated with the parameter C_2 ($C_2 = 0.3 \pm 0.15$) and the ligament diameters ($L = 44 \pm 14$ nm and 124 ± 58 , Table 1). Taking lower bounds on these parameters brings calculated values within experimental error of the measured yield stresses.

The sample annealed at 600°C has a yield strength (5.6 ± 0.6 MPa) that falls between the average and the lower bound (8.0 and 4.1 MPa) predicted by Eq. (6), using $a = 45$ and $22.5 \text{ GPa nm}^{0.86}$, $C_2 = 0.3$ and $L = 138$ nm (average value, Table 1). Annealing at 600°C healed most of the fine cracks formed during dealloying, as determined from optical microscopy observations of the sample surface after heat treatment. Thus, the measured

yield strength is likely to represent an intrinsic yield value, rather than a lower fracture stress as is probably the case for samples annealed at 100 and 300 °C. For the sample annealed at 600 °C with average ligament size of 138 nm, the ligament yield stress calculated from Eq. (2) is $\sigma_L^{YS} = 0.67$ GPa (Table 1). This high value is based on the interpolation of data from micropillar compression and nanoindentation experiments [33]. However, Jin et al. [20] and Balk et al. [21] dispute whether such high ligament yield strengths are possible in millimeter-sized, crack free np-Au. Their compression tests performed on millimeter-sized np-Au result in yield strengths almost an order of magnitude lower than those measured on np-Au by nanoindentation or compression of micropillars. Jin et al. [20] assert that, in millimeter-sized np-Au, the existence of a coherent crystal lattice among nanoligaments results in a common crystallographic slip planes much larger than the ligament diameters. This causes most ligaments to shear along these common slip planes rather than collapse individually and independently of each other, as in conventional polycrystalline foams [20]. The present gold structures with hierarchical porosity exhibit macro- and micropores, unlike the np-Au structures measured by the above authors. These macro- and micropores may act to arrest cracks and coordinated shear on a common slip plane formed during dealloying or testing, so that the true yield stress given by the intrinsic ligament strength is achieved, at least in the sample annealed at 600 °C. This result opens the door to the creation of strong, millimeter-sized np-Au.

4. Conclusions

We present a method to produce bulk (millimeter-sized in three dimensions) gold structures with three hierarchical levels of porosity (macro-, micro- and nano-porosity) produced respectively by salt replication, gas expansion and Ag dealloying. First, an Ag–19 at.% Au/NaCl composite is produced by Ag/Au/NaCl powder densification and interdiffusion at high-temperature, during which water vapor (entrapped during the densification step) is expanded to generate micropores. Then, the NaCl particles are dissolved to produce macropores. Finally, nanopores are created by dealloying the silver from the struts of the above porous Ag–19 at.% Au structures.

Annealing these gold structures with hierarchical porosity at increasing temperatures results in (i) an increase in ligament diameter from coarsening, (ii) an increase in relative density from sintering, (iii) a reduction in crack numbers (produced during dealloying) by sinter-healing. The first effect reduces the strength of the nano-ligaments and thus weakens the porous structure, while the other two effects increase its strength and ductility. A sample annealed at 600 °C, with 138 nm average ligament diameter and 74% total porosity, exhibits ductile-like behavior in compression with a yield strength in broad agreement with a model using the

high strength of gold nano-ligaments as determined from literature data on nanoindentation and micropillar compression of np-Au.

Acknowledgments

One of the authors (MEC) was supported by a National Science Foundation Graduate Research Fellowship. The authors acknowledge experimental guidance from Prof. Andrea Hodge (University of Southern California) and Mr. Reed Doucette (University of Oxford) for the dealloying procedure.

References

- [1] J. Erlebacher, R. Seshadri, *MRS Bull.* 34 (2009) 561–568.
- [2] Y. Ding, M. Chen, *MRS Bull.* 34 (2009) 569–576.
- [3] H. Jin, J. Weissmüller, *Adv. Eng. Mater.* 12 (2010) 714–723.
- [4] V. Zielasek, B. Jürgens, C. Schulz, J. Biener, M.M. Biener, A.V. Hamza, M. Bäumer, *Angew. Chem. Int. Ed.* 45 (2006) 8241–8244.
- [5] Y. Li, Y. Song, C. Yang, X. Xia, *Electrochem. Commun.* 9 (2007) 981–988.
- [6] J. Biener, G.W. Nye, A.M. Hodge, M.M. Biener, A.V. Hamza, S.A. Maier, *Adv. Mater.* 20 (2008) 1211–1217.
- [7] A. Fahmi, T. Pietsch, N. Gindy, *Macromol. Rapid Commun.* 28 (2007) 2300–2305.
- [8] G. Duan, W. Cai, Y. Luo, F. Lv, J. Yang, Y. Li, *Langmuir* 25 (2009) 2558–2562.
- [9] M.A.S. Chong, Y.B. Zheng, H. Gao, L.K. Tan, *Appl. Phys. Lett.* 89 (2006) 233104.
- [10] H. Kim, Y. Kim, *Curr. Appl. Phys.* 9 (2009) S88–S90.
- [11] W. Huang, M. Wang, J. Zheng, Z. Li, *J. Phys. Chem. C* 113 (2009) 1800–1805.
- [12] H. Zhang, J. Xu, H. Chen, *J. Phys. Chem. C* 112 (2008) 13886–13892.
- [13] G. Nye, J. Hayes, A. Hamza, J. Satcher, *Chem. Mater.* 19 (2007) 344–346.
- [14] Z. Bao, E.M. Ernst, S. Yoo, K.H. Sandhage, *Adv. Mater.* 21 (2009) 474–478.
- [15] N. Bigall, S. Hickey, N. Gaponik, A. Eychmüller, *P. Soc. Photo-Opt. Eng.* 6728 (2007), 67281N1–6.
- [16] A. Hodge, J. Biener, J. Hayes, P. Bythrow, C. Volkert, A. Hamza, *Acta Mater.* 55 (2007) 1343–1349.
- [17] C.A. Volkert, E.T. Lilleodden, D. Kramer, J. Weissmüller, *Appl. Phys. Lett.* 89 (2006) 061920.
- [18] J. Weissmüller, R. Newman, H. Jin, A. Hodge, J. Kysar, *MRS Bull.* 34 (2009) 577–586.
- [19] R. Li, K. Sieradzki, *Phys. Rev. Lett.* 68 (1992) 1168–1171.
- [20] H. Jin, L. Kurmanaeva, J. Schmauch, H. Rösner, E. Ivanisenko, J. Weissmüller, *Acta Mater.* 57 (2009) 2665–2672.
- [21] T. Balk, C. Eberl, Y. Sun, K. Hemker, D. Gianola, *JOM* 61 (2009) 26–31.
- [22] E.A. Brandes, G.B. Brook, *Smithells Metals Reference Book*, 7th ed., Butterworth-Heinemann, Boston, 1998, p. 13.71.
- [23] N.G.D. Murray, D.C. Dunand, *Acta Mater.* 52 (2004) 2269–2278.
- [24] N.G.D. Murray, D.C. Dunand, *Compos. Sci. Technol.* 63 (2003) 2311–2316.
- [25] C. Greiner, S.M. Oppenheimer, D.C. Dunand, *Acta Biomater.* 1 (2005) 705–716.
- [26] S.M. Oppenheimer, D.C. Dunand, *Mater. Sci. Eng. A* 523 (2009) 70–76.
- [27] K.N. Tu, U. Gösele, *Appl. Phys. Lett.* 86 (2005) 093111.
- [28] S. Parida, D. Kramer, C.A. Volkert, H. Rosner, J. Erlebacher, J. Weissmüller, *Phys. Rev. Lett.* 97 (2006) 035504–35514.
- [29] A. Hodge, J.R. Hayes, J.A. Caro, J. Biener, A.V. Hamza, *Adv. Eng. Mater.* 8 (2006) 853–857.
- [30] L.J. Gibson, M.F. Ashby, *Cellular Solids: Structure and Properties*, Cambridge University Press, Cambridge, 1997.
- [31] J.R. Davis, A.I.H. Committee, *Metals Handbook Desk Edition*, 2nd ed., CRC Press, Ohio, 1998, p. 626.
- [32] J. Biener, A.M. Hodge, J.R. Hayes, C.A. Volkert, L.A. Zepeda-Ruiz, A.V. Hamza, F.F. Abraham, *Nano Lett.* 6 (2006) 2379–2382.
- [33] H. Fan, D. Fang, *Mater. Des.* 30 (2009) 1441–1444.
- [34] R. Lakes, *Nature* 361 (1993) 511–515.